Impact Of Climate Change On Photovoltaic Performance: Case study in French Cities

Alexandre Mathieu, Martin Thebault, Samy Kraiem, Gilles Fraisse, Simon Thebault, Simon Boddaert, Leon Gaillard

Impact Of Climate Change On Photovoltaic Performance: Case study in French Cities

Alexandre MATHIEU[a], Martin THEBAULT[b], Samy KRAIEM[c], Gilles FRAISSE[b], Simon THEBAULT[d], Simon BODDAERT[e], Leon GAILLARD[a]

[a]*Heliocity, c/o Linksium, SATT Grenoble Alpes, 31 Rue Gustave Eiffel, 38000 Grenoble FRANCE*

[b]*LOCIE, UMR 5271, Université Savoie Mont Blanc, bât. Hélios, 60 av. du lac Léman, Savoie Technolac, 73376 Le Bourget du Lac*

[c]*CSTB, 11 Rue Henri Picherit, 44300 Nantes FRANCE*

[d]*CSTB, 24 Rue Joseph Fourier, 38400 Saint-Martin-d'Hères FRANCE*

[e]*CSTB, 290 Rte des Lucioles, 06904 Sophia Antipolis FRANCE*

Abstract

With the photovoltaic (PV) market significantly growing thanks to the support of environmental incentives, it is essential to address the influence of climate change on PV performances. In the literature, several methodologies have been suggested to measure the effect of climate change through module temperature losses and natural degradation rates, but no work has been found to combine both of them. This paper tackles this issue through a numerical approach in order to quantify to which extent climate change impacts the performance of a PV installation over its lifetime. The methodology has been applied in different French cities where climate change is found to have a moderate effect on the Performance Ratio.

Keywords: Photovoltaic performance, Climate change, Photovoltaic aging, Photovoltaic modeling

1. Introduction

Recent decades have witnessed an accelerating growth of photovoltaic (PV) capacity[1] expected to reach 14 TW by 2050 according to the 1.5 °C scenario[2] largely thanks to strong environmental incentives.[3] PV deployments rely on financial indicators such as the Levelized Cost Of Energy (LCOE) and investors need accurate predictions of PV energy production over the installation lifespan.[4] Key assumptions to this calculation are the rate of the natural PV aging and expected generation yields which are usually assumed from past observations and are likely to change due to climate change. From a general perspective, identifying potential threats to performance in future years is also crucial to forecast the energy production of PV systems.

Photovoltaic yields are intrinsically sensitive to varying environmental conditions. As described by Meng et al.,[5] the performance follows seasonal variations due to the inherent annual meteorological cycle: higher ambient air temperatures in summer relative to winter result in elevated operating temperatures and hence lower efficiencies for most PV technologies including crystalline silicon cells. Moreover, warmer sites undergo higher stresses and, logically, more pronounced degradation rates are expected than at colder sites.[6,7] Similarly, worse degradation rates have been observed on roof-mounted PV systems compared to ground-mounted[8][4] most likely because of higher operating module temperature. Through all these factors, climate change may have a significant effect on the expected performance and lifetime of solar installations.

A considerable body of works in the literature reports on the real performance and degradation of PV systems. For instance, the IEA compiled performance variables in their hosted IEA PVPS Performance Database[9] and Jordan et al. made available open-source databases on measured degradation rates.[6,10] From two separate analyses, a typical reference performance ratio of around 76 % was reported[11,12] and an average performance loss rate in the order of magnitude of 0.5 % have been highlighted.[10,11] All these studies suggest performance benchmarks based on historical PV systems, and yet none offer correction factors to adjust those expectations in the context of climate change.

By means of climates scenarios, PV potential has been investigated around the world[13].[14] Historical trends have been identified in degradation models with an increase in degradation rate following the increase of the world ambient temperature on the ERA5 dataset.[15] The impact of climate change on the performance ratio due to higher instantaneous temperature losses has been quantified to less than 3% in 2100 for different world locations by Ascencio-Vasquez et al..[16] However, the combined detrimental effects of climate change on degradation rates and the instantaneous-temperature performance dependency have never been investigated together. This paper addresses this issue by combining climate change scenarios and PV models which include natural aging to enable a more rigorous approach to project long-term PV performance.

The aim of this article is to project PV performance over a typical 30-year installation lifetime taking into account the EURO-CORDEX climate projections following the RCP 8.5 scenario and quantify the impact of climate change in different cities in France. In the presented study cases in France, a slight drop in performance is observed mainly because of more module temperature losses and enhanced aging mechanisms. The methodology is established through a model chain to propagate climate projections in order to derive PV performance on different climate periods in Section 2. Then, results are outlined in Section 3, first, with the study case of Bordeaux, France, and, then, on some other French cities.

2. Methodology

Figure 1 shows the general methodology presented in this paper in order to evaluate the Performance Ratio PR taking into account the climate changes. First, climate projections are built in order to get the weather time series from 1990 up to 2080 (see Section 2.1). Decomposition/transposition, IAM/SMM/soiling, humidity, UV, module temperature, power, degradation and inverter models (sections 2.2, 2.3, 2.4, 2.5, 2.6, 2.7, 2.8, 2.9) mostly supported with pvlib[17] enable then to calculate the effect of these variables on the PV system operation. From there, the instantaneous performance as well as the degradation due to aging can be evaluated which *in fine* allows to evaluate the PR in Section 2.10.

Three periods are investigated, a reference period ranging from 1990 to 2020 as the close past, a near future corresponding to 2020-2050, and a far future, from 2050 to 2080.

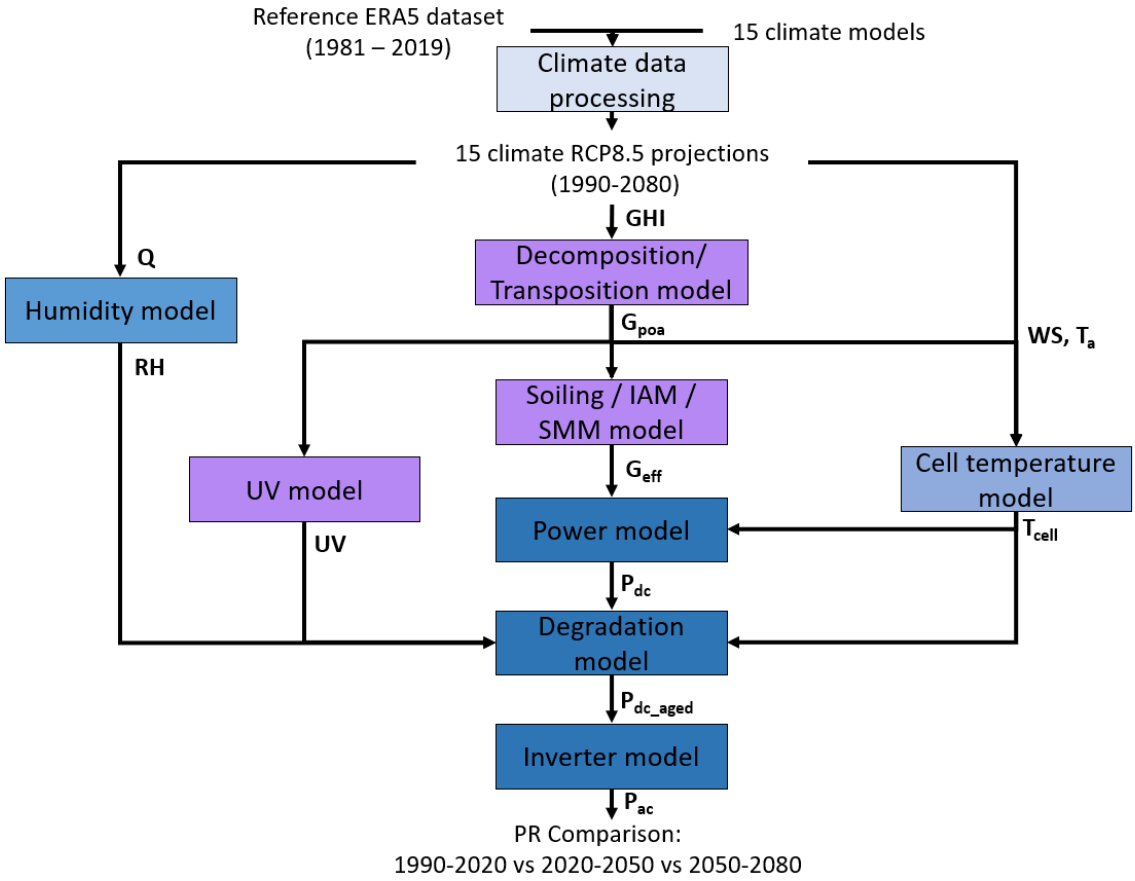

Figure 1: Model chain methodology to assess climate change impact on PV performance

2.1. Climate data

This Section describes the process to obtain climate projections at the hourly resolution for the following variables: global horizontal irradiance, ambient air temperature, specific humidity, atmospheric pressure and wind speed.

2.1.1. Data sources

Historical reference data and climate models are used to create hourly climate projections and Table 1 summarizes the characteristics of the two

used data sources.

	EURO-CORDEX 11	**ERA5**
Data type	Climate models	Historical reference data
Grid resolution	0.11°	0.25°
Scenario	RCP 8.5	-
Time step	three-hourly	hourly
Periods of interest	1950 - 2100	1981 - 2019

Table 1: Data source description: EURO-CORDEX and ERA5

In order to build up climate projections, 15 models from the EURO-CORDEX-11 ensemble[18,19] were retrieved and are further described in Table 6 in Appendix A.1. The RCP 8.5 scenario, which is one of the most pessimistic, corresponds to an additional radiative forcing of 8.5 W/m2 in 2100 and has been chosen for the projections to study the worst-case degradation configuration.

Nonetheless, the outputs of the EURO-CORDEX models are often far from real conditions[20] and need to be modified according to the location with bias-correction methods taking the ERA5 dataset[21] as a reference on 1981-2019.

2.1.2. Bias correction

In order to correct the bias in climate model outputs, two bias correction methods of the quantile-quantile correction type were chosen: the CDF-t (Cumulative Density Function - transform)[22] and the Q-MAP method.[23–25] The general principle is to correct the distribution of a variable of the model output with support of the ERA5 distribution of the same variable on 1981-2019 quantile by quantile. In order not to lose the thrust of the article, these

essential aspects are presented in Appendix A.

The CDF-t method[22] is especially applied to correct temperature, specific humidity, pressure, radiation, and wind speed data with the reference period taken from 1981 to 2019. Each variable is adjusted independently of the others.

2.1.3. Hourly interpolation

Once the three-hourly data from the EURO-CORDEX models have been bias-corrected, they are post-processed to obtain hourly time series. In order to do so, a Hermite cubic interpolation[26,27] is used to temporally refine the data to get them ready to be injected in the next models.

2.2. Decomposition and transposition models

In this section, the process to obtain the irradiance in the plane of array from the global horizontal irradiance provided from the climate projections is described.

2.2.1. Decomposition model

Decomposing the Global Horizontal Irradiance (GHI) into Direct Normal Irradiance (DNI) and Diffuse Horizontal Irradiance (DHI) is a crucial step to estimate the irradiance received by the photovoltaic installation. The DIRINT model[28] is adopted to decompose the irradiance and needs as inputs the absolute airmass AM_{abs}, the angle of incidence AOI and the extraterrestrial Direct Normal Irradiance DNI_{extra} to deduce the clearness index.

The Spencer model[29] enables to calculate the DNI_{extra} with the solar constant equal to 1370 W/m^2. The relative airmass AM_{rel} is calculated by the Kasten model[30] and the altitude of the installation is deducted from the

EU-DEM database.[31] The absolute airmass AM_{abs} is then deducted from the relative airmass AM_{rel} and the pressure P with $AM_{abs} = AM_{rel}\frac{P}{101325}$. The sun elevation and azimuth are then estimated thanks to the NREL algorithm[32] with the altitude and taking the ERA5 temperature and pressure averages on 1981-2019 as the reference ambient temperature and pressure. Then, the angle of incidence AOI is derived according to the following equation with z the sun elevation, β the installation tilt, ϕ_a the sun azimuth and ϕ the installation azimuth

$$cos(AOI) = cos(z)cos(\beta) + sin(z)sin(\beta)cos(\phi_a - \phi). \quad (1)$$

The DIRINT model from Perez et al.[28] can then applied to estimate the DNI component. Then, the DHI component is deducted thanks to the following formula with AOI the angle of incidence and GHI the global horizontal irradiance

$$DHI = GHI - DNI \cdot cos(AOI). \quad (2)$$

2.2.2. Transposition model

The obtained decomposed irradiance components enable the transposition models to calculate the received irradiance in the plane of array of the installation. AM_{rel}, DNI_{extra}, solar zenith and azimuth can be processed together to calculate the diffuse irradiance component thanks to the Perez model[33] with the following equation

$$G_{POA,d} = DHI \cdot [(1 - F1) \cdot \frac{1 + cos(AOI)}{2} + F1 \cdot \frac{a}{b} + F2 \cdot sin(AOI)]. \quad (3)$$

where:

- $F1$,$F2$ are empirically fitted functions describing the circumsolar and horizon brightness respectively computed from the airmass and relative airmass [-]
- DHI the diffuse horizontal irradiance $[W/m^2]$
- $a = max(0, cos(AOI))$ with AOI, the angle of incidence [-]
- $b = max(cos(85, cos(z))$ with z the solar zenith angle [-]

Then, the direct beam irradiance can be directly obtained from the Direct Normal Incidence DNI irradiance and the sun angle of incidence AOI from the following equation

$$G_{POA,b} = DNI \cdot cos(AOI). \tag{4}$$

Assuming an isotropic reflection from the ground, the ground-reflected irradiance component follows the next equation with the module tilt angle β and ρ the albedo set to 0.18 in this study for an urban environment according to PVsyst assumptions.[34]

$$G_{POA,alb} = GHI \cdot \rho \cdot \frac{1 - cos(\beta)}{2}. \tag{5}$$

Finally, the total POA irradiance is the sum of the direct, reflected and diffuse components.

$$G_{POA} = G_{POA,b} + G_{POA,alb} + G_{POA,d} \tag{6}$$

2.3. Effective irradiance models

The characteristics of the outdoor irradiance are different from STC conditions and the Soiling Ratio SR, the Indice Angle Modifiers (IAM_b, IAM_d, IAM_{alb}) and the Spectral Mismatch Modifier SMM are indices which enable to express those differences and calculate the effective irradiance G_{eff} received by the module.

2.3.1. Indice Angle modifier model

The Indice Angle modifier (IAM) computes the reflection losses on the module and is calculated using the approach from Martin et Ruiz.[35]

$$G_{POA,iam} = G_{POA,b} \cdot IAM_b(AOI) + G_{POA,d} \cdot IAM_d(\beta) + G_{POA,alb} \cdot IAM_{alb}(\beta) \tag{7}$$

$G_{POA,iam}$ is the irradiance which includes the reflection losses and is obtained by applying the Indice Angle Modifiers (IAM_b, IAM_d, IAM_{alb}) respectively to the direct, diffuse and ground-reflected irradiance in the plane of array. IAM_b is function of the angle of Incidence (AOI) while IAM_d, IAM_{alb} depend on the PV tilt β. The m-Si parameters from Martin and Ruiz's study[35] have been injected in the different IAMs modifier models.

2.3.2. Soiling loss model

The effect of the accumulation of soiling on the PV modules can be expressed through the Soiling Ratio SR which corresponds to the transmission loss in this study. The soiling mechanisms are fairly complex to model[36] and the approach from Kimber et al.[37] enables to simplify its influence with the following formula :

$$SR = 1 - d \cdot sr_{daily}. \tag{8}$$

with:

- sr_{daily} the daily soiling rate which is equal to $0.15\%/day$, inspired from Kimber's study[37] which is around the median of the estimated soiling rate for France according to Ilse et al..[36]
- d, the number of days since the last rainfall episode which is assumed to fully clean the PV modules.

Among all cleaning thresholds presented in the literature, 5mm was chosen since it is similar to some thresholds in the same climate Koppen zone, Cfb, as Bordeaux from the literature summary from Bessa et al.[38] No grace period has been assumed after a rainfall episode, the soiling rate starts to reduce the transmission right the day after it.

2.3.3. Spectral Mismatch Modifier model

The mismatch between the irradiation received by the module and the effective spectrum converted by the photovoltaic cell are calculated using the Spectral Mismatch Modifier (SMM) obtained with the approach from Lee et Panchula[39] relying on the SMARTS model.[40]

$$SMM = c_1 + c_2 \cdot AM_{abs} + c_3 p_w + c_4 AM_{abs}^{0.5} + c_5 p_w^0 .5 + c_6 \frac{AM_{abs}}{p_w^{0.5}}. \tag{9}$$

where:

- The absolute airmass AM_{abs} is deducted from the AM_{rel} as seen in the previous section 2.2
- The precipitable water p_w corresponds to the amount of water contained in a column of air available for potential rainfall. This variable is obtained from the ambient temperature and relative humidity following the model from Gueymard et al..[41]
- The empirical parameters $c_1, c_2, c_3, c_4, c_5, c_6$ are provided from First Solar[39] for mono-crystalline modules in pvlib.[17]

The SMM and SR can then be applied on top of the IAM operation to obtain the effective irradiance as follows,

$$G_{eff} = G_{POA,iam} \cdot SR \cdot SMM. \tag{10}$$

2.4. Relative humidity model

The infiltration of humidity in PV modules might decay module performances through delamination or corrosion and it is then essential to quantify it to later introduce it as input in degradation models in Section 2.8. The relative humidity RH can be calculated using Bolton's formulation[42] with Q the specific humidity, T the temperature $[°C]$, and P the pressure $[hPa]$. First, the saturation vapor pressure e_s $[hPa]$ is defined

$$e_s = 6.112 \cdot \exp(\frac{17.67 \cdot T}{T + 243.5}). \tag{11}$$

The water vapor pressure e $[hPa]$ is calculated with the following formula

$$e = \frac{Q \cdot P}{0.378Q + 0.622}. \tag{12}$$

Finally, the relative humidity [%] is obtained as follows

$$RH = \frac{e}{e_s}. \tag{13}$$

2.5. UV model

Quantifying the quantity of UV absorbed by the PV modules is essential to later assess the degradation due to photon absorption. As for modeling perspectives, the same approach as Kaaya et al[43] and Ascencio et al.[15] is adopted with the model from Crommelynck and Joukoff.[44] The Linke Turbidity factor is inferred from a world map[45] from SODA and daily interpolated.[17] Then, the clear sky components are obtained with the Ineichen model.[46] The clearness indicator is then deducted from the GHI and its corresponding clear sky $GHI_{clearsky}$ as follows.

$$k_t = max(0.1, min(0.7, \frac{GHI}{GHI_{clearsky}})) \tag{14}$$

The UV is further computed from the UV-A and UV-B components

$$UV = UV_A + UV_B, \tag{15}$$

$$UV_B = (1.897 - 0.860 \cdot k_t)1e^{-3} \cdot G_{POA} \tag{16}$$

$$UV_A = (7.210 - 2.365 \cdot k_t)1e^{-2} \cdot G_{POA}. \tag{17}$$

2.6. Temperature model

The module temperature is subject to material properties and weather conditions. The Faiman model[47] enables to integrate those interactions and

estimates T_m the module temperature [$°C$] with the following equation

$$T_m = T_a + \frac{G_{POA}}{U_0 + U_1 \cdot WS}, \tag{18}$$

with T_a the ambient temperature [$°C$], G_{POA} the irradiance in the plane of array [W/m^2], $WS[m/s]$ the wind speed, U_0 [$\frac{W}{m^2K}$] and U_1 [$\frac{W}{m^2K(m/s)}$] empirical constants translating the constant and convective heat transfer components.

Following the same approach as Kaaya et al.,[48] the thermal coefficients $U_0 = 26.9\ \frac{W}{m^2K}$, $U_1 = 6.2\ \frac{W}{m^2K(m/s)}$ have been adopted from the outdoor calibration conducted by Koehl et al.[49] on an open-rack mono-crystalline module with a polymer backsheet.

2.7. Power model

Power models estimate the DC electric output according to site characteristics and weather variables. The PVWatts model[50] is chosen in this study and estimates the instantaneous DC power P_{dc} at time t as

$$P_{dc}(t) = G_{eff}(t) \cdot \frac{P_0}{G_{ref}} \cdot (1 - \gamma \cdot (T_c(t) - T_{ref})), \tag{19}$$

where, $T_c(t)$ is the cell temperature [°C] here approximated as the module temperature $T_m(t)$, $G_{eff}(t)$ is the effective irradiance in the plane of array [W/m^2], T_{ref} and G_{ref} are the Standard Test Conditions respectively equal to $25°C$ and $1000W/m^2$, P_0 is the DC rated power [Wp], γ is the efficiency loss coefficient arbitrary set, in this study, to a pessimistic 0.45 $\%/K^{-1}$. This high coefficient value has particularly been chosen in order to keep a worst-case dimensioning perspective to the study.

2.8. Degradation model

Commonly approximated as linear, outdoor monitoring have shown that some degradation rates are actually non-linear.[10] To that aim, Kaaya et al.[43][51] suggested an exponential degradation model accounting for the dominating stressors: temperature, UV irradiation, relative humidity, and temperature cycling.[52] The cumulative degradation η_{kaaya} is computed for a calendar year y as

$$\eta_{kaaya}(y) = 1 - exp(-(\frac{\Gamma}{k \cdot (y - y_0)})^{\mu}) \tag{20}$$

where k is the total degradation rate, y_0 is the installation year and (Γ, μ) are empirical constants. In this approach[43],[51] the total degradation rate k depends on yearly environmental conditions and is broken down into three degradation processes k_H, k_P, k_{T_m} as follows with

$$k(y) = A_N \cdot (1 + k_H(y)) \cdot (1 + k_P(y)) \cdot (1 + k_{T_m}(y)) - 1. \tag{21}$$

1. k_H the hydrolysis-driven degradation:

$$k_H = A_H \cdot RH^n \cdot exp(-\frac{E_{ah}}{k_B \cdot T_{mod}}) \tag{22}$$

2. k_P the photo-degradation:

$$k_P = A_p \cdot UV^X \cdot (1 + RH^n) \cdot exp(-\frac{E_{ap}}{k_B \cdot T_{mod}}) \tag{23}$$

3. k_{T_m} the thermo-mechanical degradation:

$$k_{T_m} = A_t \cdot C_N \cdot (273 + \Delta T)^{\theta} \cdot exp(-\frac{E_{at}}{k_B \cdot T_{max}}) \tag{24}$$

where:

A_N the normalization constant $[year^{-2}]$, set to 1 by default

$E_{ah}E_{ap}E_{at}$ the activation energies of power degradation due to hydrolysis, photo-degradation and thermo-mechanical mechanism respectively, in $[eV]$

$A_hA_pA_t$ the pre-exponential constants, respectively in $[year^{-1}]$, $[m^2/kWh]$, $[^\circ C^{-1}cycle^{-1}]$

k_B the Boltzmann constant $(8.62 \cdot 10^{-5} eV/K)$

n,X,θ empirical constants that indicate the impact of relative humidity, UV and temperature cycle on power degradation

RH the relative humidity [%]

T_{mod} average module temperature $[K]$

$\Delta T = T_{max} - T_{min}$ the temperature difference $[K]$

$T_{max}T_{min}$ the module maximum and minimum temperatures taken as 5th and 95th quantiles of the hourly distribution over the year y. $[K]$

C_N cycling rate $[cycles/year]$, the yearly temperature cycling frequency

The parameters have been deducted from Kaaya's study[43] from aging tests for a classic mono-crystalline module with glass/polymer sandwich with aluminum frame and are gathered in the following table.

Degradation Sub-process	Pre-exponential constants	Model parameters	Activation energies
Hydrolysis	$A_h = 4.91e7\ year^{-1}$	$n = 1.90$	$E_{ah} = 0.74\ eV$
Photo-degradation	$A_p = 71.83\ m^2/kWh$	$X = 0.63$	$E_{ap} = 0.45\ eV$
Thermo-mechanical	$A_t = 2.04\ ^\circ C^{-1}cycle^{-1}$	$\theta = 2.24$	$E_{at} = 0.43\ eV$

Table 2: Parameters from Kaaya et al.[43]

In past studies,[15,16,43,51] the degradation was evaluated based on constant weather conditions, and kept constant for the entire lifespan of the PV system. Following this approach, the sub-degradation rates are calculated for each year and the averages over the 30-year period are taken to calculate the total degradation rate k in Equation 21 to inject into Kaaya's model.

Then, this degradation factor is applied to calculate the aged DC power at all times t which belongs to year y as follows,

$$P_{dc,aged}(t) = P_{dc}(t) \cdot \eta_{ageing}(y) \tag{25}$$

2.9. Inverter model

The inverter model calculates the efficiency to convert DC power to AC and has been implemented with the PVwatts model[50] with the typical reference value $\eta_{ref} = 0.9637$ and $\eta_{nom} = 0.96$ as in the equation below

$$\eta_{inv} = \frac{\eta_{nom}}{\eta_{ref}}(-0.0162 \cdot \zeta - \frac{0.0059}{\zeta} + 0.9858). \tag{26}$$

where:

- P_{ac0}, the AC rating power is determined from the DC-to-AC ratio of the system, assumed to a generic 1.2 in this study (ie. $P_{ac0} = 0.83$ kWp if the DC rating power is 1 kWp)
- $\zeta = \frac{P_{dc}}{P_{dc0}}$ with $P_{dc0} = \frac{P_{ac0}}{\eta_{nom}}$

Then the AC power output is computed such as

$$P_{ac} = \min(\eta P_{dc}, P_{ac0}). \tag{27}$$

2.10. Definition of the Performance Ratio

To compare the installation on different climate periods, the PV performance is evaluated over a period of time T, typically a year y or a *period* of 30 years in this study, through the Performance Ratio (PR) defined as in the IEC 61724-1[53]

$$PR(T) = \frac{E(T)}{E_{POA}(T)} / \frac{P_0}{G_{ref}}, \tag{28}$$

where $E(T) = \int_T \cdot P_{ac}(t)\, dt$ is the energy output $[Wh]$ from the PV system over time T, $E_{POA}(T)$ is the total irradiation received from the sun in the plane-of-array $[Wh/m^2]$ over time T, P_0 is the installation DC rated power in Wp and $G_{ref} = 1000\ W/m^2$ the reference irradiance.

In the next section, the PR is going to be evaluated and broken down into two parts: η_{ageing} and the instantaneous part only, $PR_{instant}$ which will be calculated as if aging had no effect with $\eta_{ageing}(y) = 1$ over the whole period.

3. Results

To assess the impact of climate change on PV systems, climate projections are injected into the model chain previously presented and PV performances are analyzed on 1990-2080.

3.1. Bordeaux study-case

The location of Bordeaux, France (44.837789, -0.57918) has been selected to model an installation of a 1 kWp system, facing south with a 30° tilt. The 15 hourly climate projections generated with respect to the RCP 8.5 scenario according to the methodology in Section 2.1 for Bordeaux are first described and the installation performances are then investigated.

3.1.1. Description of the climate projections

The evolution of the main variables affecting the PV performances of the 15 climate projections are studied in this section. In order to distinguish the main trends over the different periods, the variables are first yearly aggregated (taking the average for temperature and humidity and the sum for irradiations), and, then, the 30-year average on each future period is compared to the 1990-2020 average for all projections on Table 3.

Different trends can be identified for the different stressors. The ambient temperature increases significantly over each period for all climate projections. Regarding the evolution of irradiation and UV exposure over time, there is no strict consensus among all projections but the median tends to slightly increase. As for the relative humidity, the whole distribution tends to slightly decrease overall except for one projection per period which increases.

		2020-2050	2050-2080
Ambient temperature [$°C$]	minimum	+0.4	+1.6
	median	+0.9	+2
	maximum	+1.3	+2.7
In-Plane irradiation [$kWh/m2/year$]	minimum	-12	-31
	median	+15	+28
	maximum	+61	+76
In-plane UV exposure [$kWh/m^2/year$]	minimum	-0.6	-1.7
	median	+0.7	+1.4
	maximum	+3.2	+4.0
Relative humidity [%]	minimum	-1.4	-2.2
	median	-0.4	-1.1
	maximum	+0.1	+0.1

Table 3: Evolution of the distribution of the main climate variables for all 15 climate projections for each period compared to the 1990-2020 period

In regards to the main PV stressor, the temperature variations of all climate projections are shown in Figure 2. The hourly module temperature is filtered when the irradiance is non-null and the yearly average (orange), 5th quantile (yellow), and 95th quantile (red) are computed for all projections. Those variables are then compared to the variations of the yearly averaged ambient temperature (blue) similarly filtered over daytime. Overall, the yearly averaged module temperature shares the same trends as for the yearly averaged ambient temperature with a rough 2°C increase for the projection median over 2050-2080 compared to 1990-2020. However, the 5th and 95th module temperature quantiles increase by around 1.5°C and 3.5°C respectively on average on 2050-2080 compared to 1990-2020 and accelerate the thermo-mechanical processes due to greater temperature cycles.

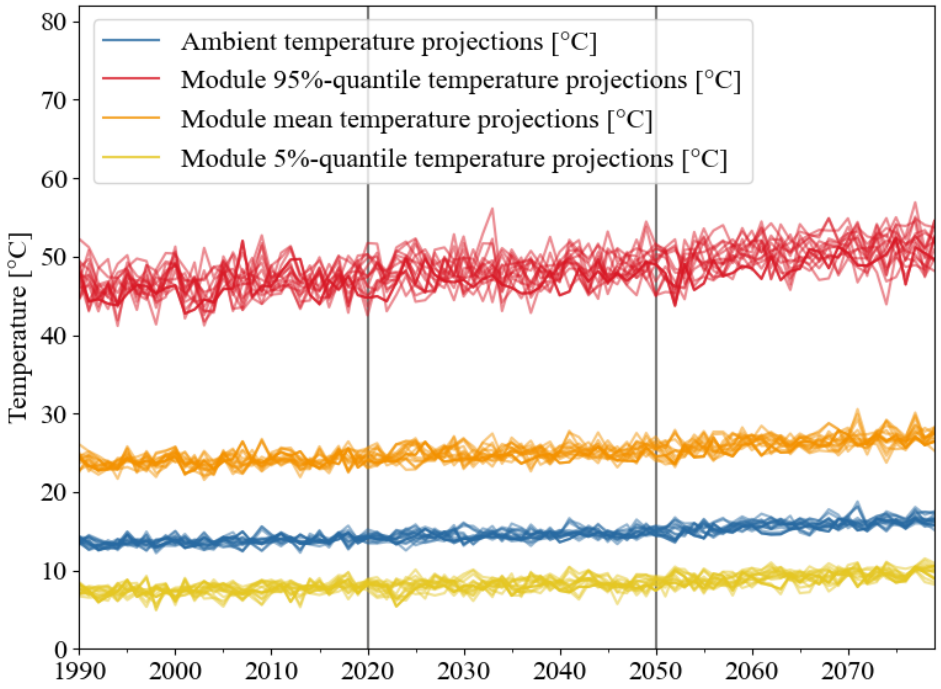

Figure 2: Yearly daytime module and ambient temperatures for all projections on 1990-2080

3.1.2. Evolution of the performance over time

After having analyzed the evolution of the climate projections over 1990-2080 in the previous section, the performance of the installation being installed in 1990, 2020, and 2050 is projected over 30 years and investigated in this section.

The installation performance which includes IAM, SMM, soiling, temperature and inverter losses is first studied through $PR_{instant}$ while setting $eta_{ageing}(y) = 1$ as defined in Section 2.10. For each projection p, $PR^{p}_{instant}(y)$

is calculated for every year y and is plotted in Figure 3 over the 2020-2050 (red) and 2050-2080 (orange) periods. On another note, the historical $PR_{instant,hist} = 88.1$ % (in black) corresponds to the yearly averaged $PR_{instant}$ over the 1981-2019 period obtained from the ERA5 dataset. Due to the natural climate variability, some of the future years are still colder than the historical average and would lead to a higher $PR^{p}_{instant}(y)$ than $PR_{instant,hist}$. On the other hand, in average, other years have hotter temperature and result in the opposite effect with a lower value than the historical one.

In contrast to the expected rise of temperature, the distance of $PR^{p}_{instant}(y)$ to $PR_{instant,hist}$ stays small when comparing projections to historical values at Bordeaux. The averaged $PR^{p}_{instant}(y)$ projection (red dots) on 2020-2050 decreases by 1.0 % after 30 years compared to the historical $PR_{instant,hist}$ and drops by 2.2 % in 2080 for the period 2050-2080 (orange dots).

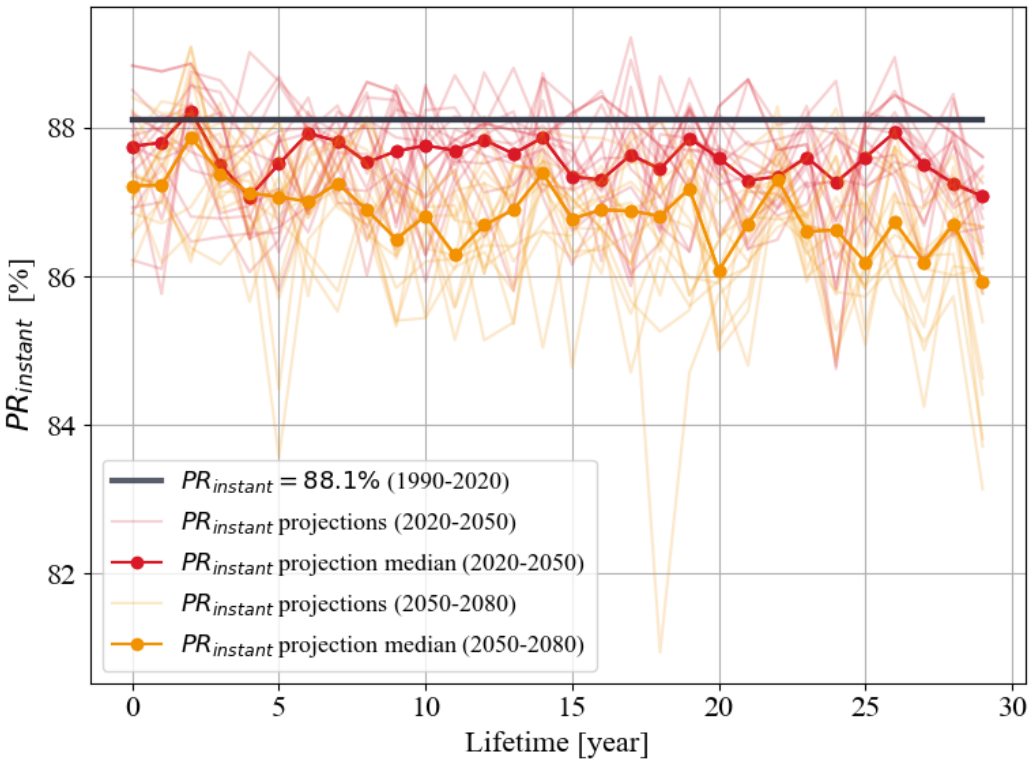

Figure 3: $PR_{instant}$ over time of 15 climate projections on 2020-2050 and 2050-2080 at Bordeaux

The worst yearly performances are reached with the projection p =ICHEC-EC-EARTH-SMHI-RCA4-r1i1p1-rcp85 for the 2020-2050 period and with the projection p =IPSL-IPSL-CM5A-MR-SMHI-RCA4-r1i1p1-rcp85 for the 2050-2080 period. As shown in Table 4, those bad performances are particularly reached during hot years with long drought periods over summer where the production is at its highest peak and is reduced because of high soiling losses.

Year	**Climate projection**	$PR_{instant}$	**Average ambient temperature**	**Longest period without rainfall over 5mm between March-November**
1991-2019	ERA5 dataset	88.2% °C (average over 1991-2019)	13.7 °C (average over 1991-2019)	62 days (longest period over 1991-2019)
2044	ICHEC-EC-EARTH-SMHI-RCA4	81.8%	15.6 °C	82 days
2068	IPSL-IPSL-CM5A-MR-SMHI-RCA4	85.8%	17.33°C	161 days

Table 4: Worst performances over 2020-2050 and 2050-2080 compared to ERA5 dataset

The $PR_{instant}$ variations from year to year of the climate projections also seem to increase compared to the historical $PR_{instant,hist}$ variations. Especially, the ERA5 historical standard deviation is 0.52%, and the median over all 15 climate projection standard deviations increases to 0.65% over 2020-2050 and to 0.83% on 2050-2080. Then, the performance decreases but also varies more from year to year because of climate change.

In regards to aging, the distribution of the 30-year averaged degradation rate k^{p}_{30year} for all projections is shown in Figure 4 for each climate period. The degradation coefficient k_{30year} increases slightly over each period and this trend is the result of the increase of all individual degradation sub-processes $k_{H,30year}$, $k_{P,30year}$, $k_{T_m,30year}$.

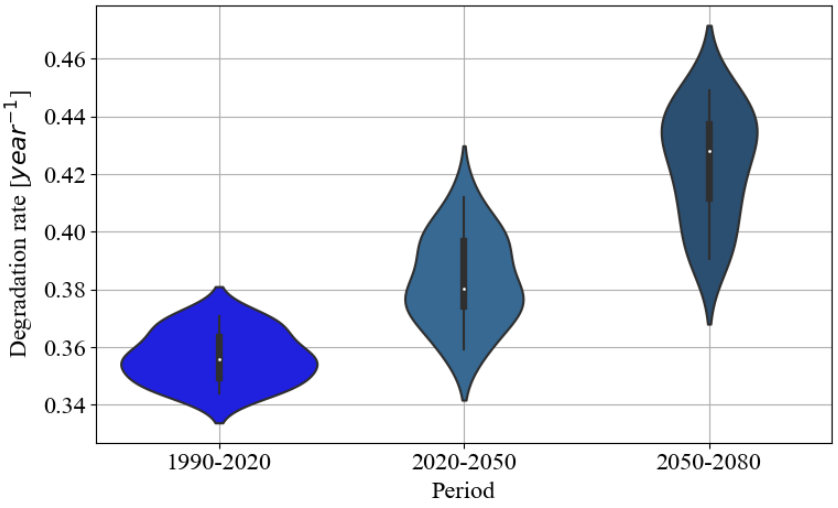

Figure 4: Degradation rate k_{30year} distribution on different climate periods

In Figure 4, the aging component $\eta^{p}_{aging}(y)$ is calculated for every single projection p on 2020-2050 (red) and 2050-2080 (orange). The historical trend (black) $\eta_{aging,hist}$ has been calculated by injecting the ERA5 1981-2019 historical averaged degradation rate $k = 0.37\ year^{-1}$ in Kaaya's model presented in Section 2.8. Overall, the difference between the climate projections and the historical trend is rather small. The averaged $\eta^{p}_{aging}(y)$ over the projections accounts for a decrease of only 0.2% after 30 years on 2020-2050 and 0.9% after 30 years on 2050-2080.

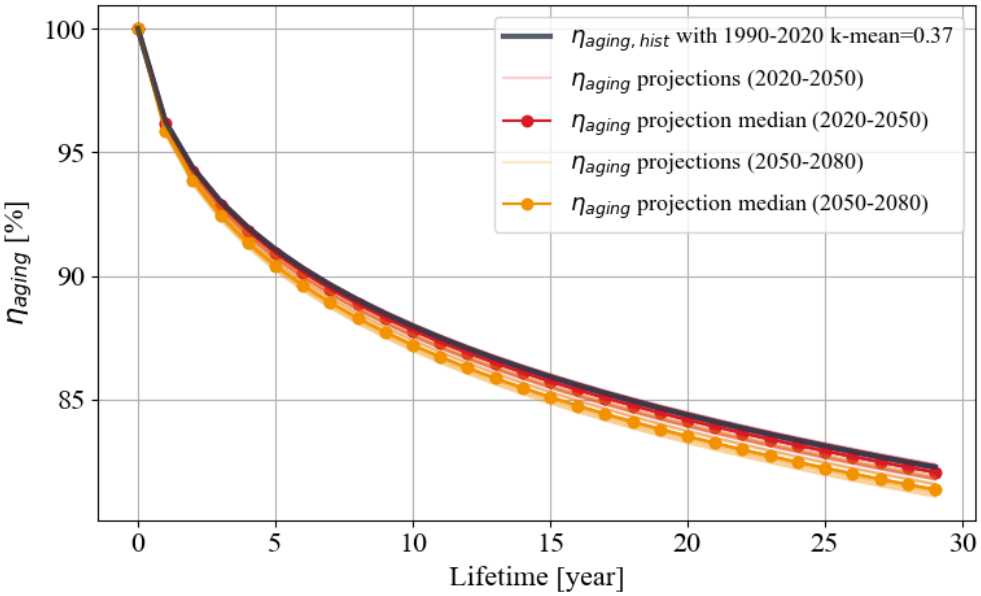

Figure 5: η_{aging} over time of 15 climate projections on 2020-2050 and 2050-2080 at Bordeaux

When correctly applying aging to calculate the PR for each year as in Equation 28 for each projection p, $PR^p(y)$ decreases over the future periods as shown in Figure 6. Compared to the historical $PR_{hist}(y)$ defined as the product of $\eta_{power,hist}$ and $\eta_{aging,hist}(y)$, the $PR^p(y)$ average is decreased by 1.1 % and 2.5 % after 30 years for the time period 2020-2050 and 2050-2080 respectively.

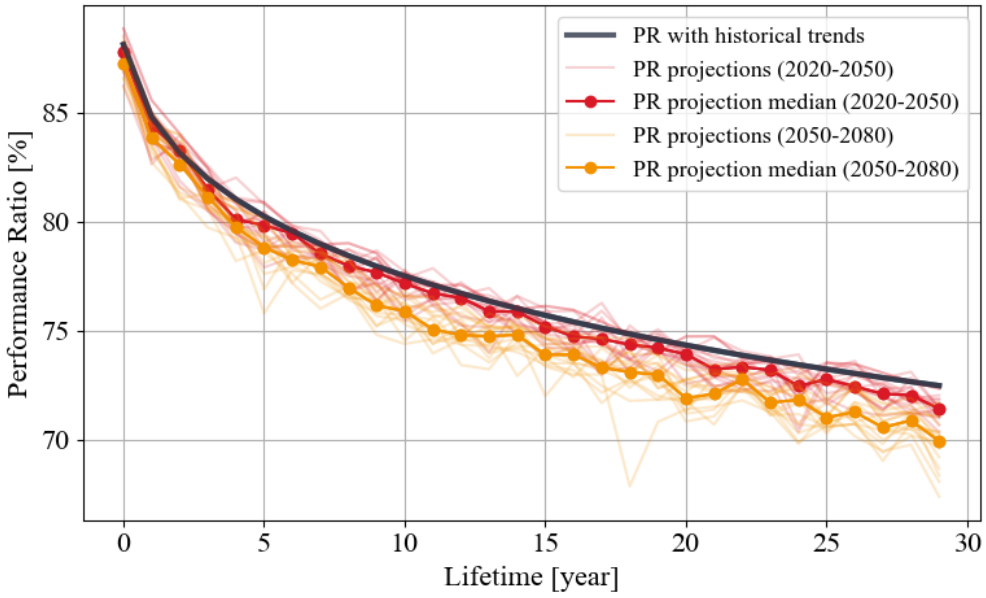

Figure 6: Evolution of the PR in Bordeaux, for all 15 climate projections on the time period 2020-2050 and 2050-2080

3.1.3. Lifetime performance

From a lifetime perspective, the performance of the installation can also be calculated by integrating the PV energy output and received irradiation over the whole 30-year period as defined in Equation 28 for each projection p and *period* (1990-2020, 2020-2050 or 2050-2080) to get $PR^{p}_{30year}(period)$. Figure 7 offers then an alternative representation, as a violin distribution plot (similar to a y-centered density curve, the width representing the frequency of data points in each region), of the PR_{30year} for all climate projections on the three periods under study.

Due to climate change, the median of the $PR^{p}_{30year}(period)$ distribution

over the projections tends to decrease from 77.1 % for the 1990-2020 period through 76.4 % on 2020-2050 to 75.1 % on 2050-2080. On the other hand, the spread between the minimal and maximal $PR^{p}_{30year}(period)$ over the 15 projections slightly increases starting with a range spread of 0.7 % on 1990-2020, 1.2 %on 2020-2050 and 1.9 % on 2050-2080. This particularly emphasizes more uncertainty associated to more future periods.

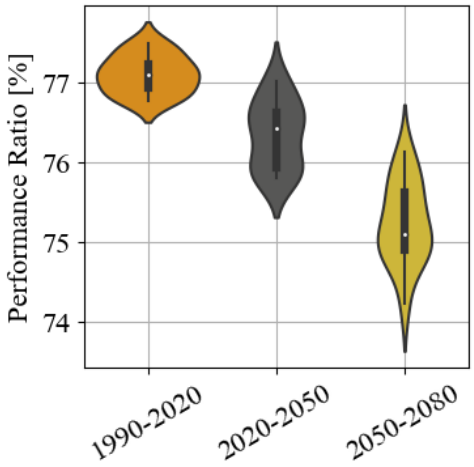

Figure 7: Violin density plots of the PR for the 15 climate projections on the three periods under study at Bordeaux

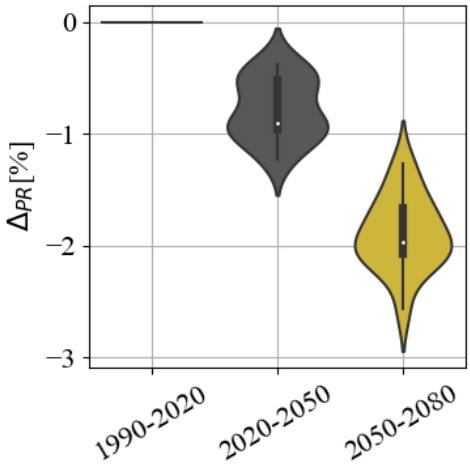

Figure 8: Violin density plots of the Δ_{PR} for the 15 climate projections on the three periods under study at Bordeaux

To show how the projection performances vary over each period relatively to the recent past period 1990-2020, Figure 8 displays the relative $\Delta^{p}_{PR}(period)$ for every trajectory p defined as $\Delta^{p}_{PR}(period) = PR^{p}_{30year}(period) - PR^{p}_{30year}$(1990-2020). The variations are still limited compared to the absolute PR_{30year} with a median decreasing by 0.9 % on 2020-2050 and 2.0 % on 2050-2080 compared to 1990-2020.

3.1.4. Loss breakdown evolution over time

In order to better understand the evolution of the performance over time, each individual loss is analyzed. To that aim, the IAM, soiling, inverter, temperature, aging losses and spectral correction (SMM) are calculated over the installation lifetime for each climate period as follows.

- IAM losses are a function of the irradiation $G_{POA,iam}$ including the indice angle modifications and the global irradiance in the plane of array G_{POA}:

$$IAM_{loss} = 1 - \int G_{POA,iam}(t)\ dt / \int G_{POA}(t)\ dt \tag{29}$$

- SMM losses are calculated as a function of the Spectral Mismatch Modifier SMM, $G_{POA,iam}$ and G_{POA}:

$$SMM_{loss} = 1 - \int G_{POA,iam}(t) \cdot SMM(t)\ dt / \int G_{POA}(t)\ dt \tag{30}$$

- Soiling losses are calculated as a function of the Soiling Rate SR, $G_{POA,iam}$ and G_{POA}:

$$Soiling_{loss} = 1 - \int G_{POA,iam}(t) \cdot SR(t)\ dt / \int G_{POA}(t)\ dt \tag{31}$$

- Temperature losses are calculated as a function of the effective irradiation $G_{POA,eff}$, the temperature coefficient γ and the module temperature T_{mod}:

$$Temp_{loss} = \int G_{POA,eff}(t) \cdot \gamma \cdot (T_{mod}(t) - 25^{\circ})\ dt / \int G_{POA,eff}(t)\ dt \tag{32}$$

- Ageing losses are calculated as a function of the non-aged and aged DC power, respectively P_{dc} and $P_{dc,aged}$:

$$Ageing_{loss} = 1 - \int P_{dc,aged}(t)\ dt / \int P_{dc}(t)\ dt. \tag{33}$$

- Inverter losses are calculated as a function of the AC power P_{ac} and the aged DC power $P_{dc,aged}$:

$$Inverter_{loss} = 1 - \int P_{ac}(t) dt / \int P_{dc,aged}(t)\ dt. \tag{34}$$

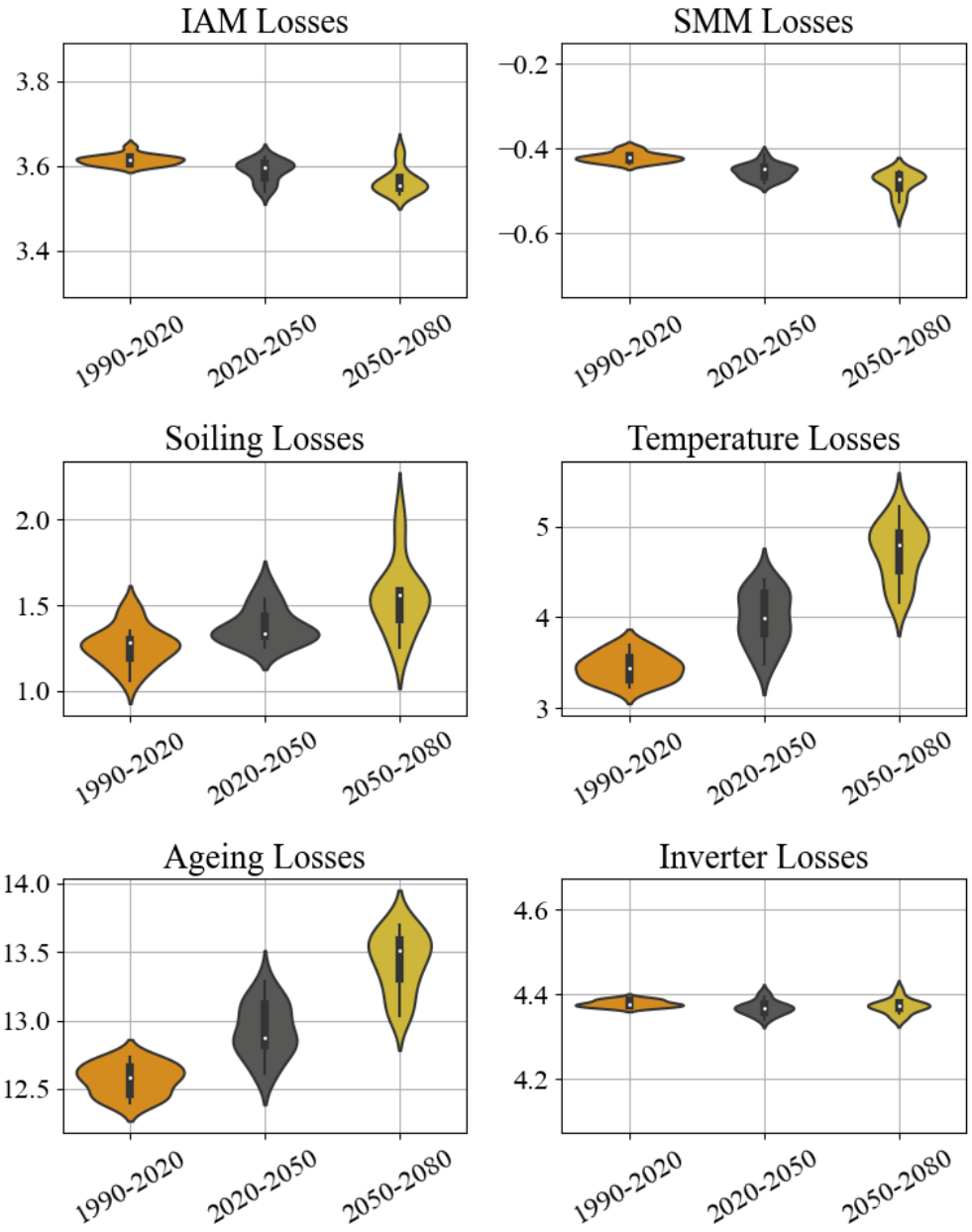

Figure 9: Losses for all 15 climate projections on the three periods under study at Bordeaux

413 The different losses have been calculated for each climate period as shown

in Figure 9 and have different trends over time.

- The IAM losses tend to very slightly decrease over time. Among all projections, there is a slight tendency for the share of the direct irradiation over the global irradiation to increase. Following Martin and Ruiz's approach[35] to calculate the IAM loss factors as described in Section 2.3.1, the loss coefficient for the direct irradiance component is lower than the diffuse and the ground factors in average. Then, the overall reflection losses tend to very slightly decrease since the share of the irradiation being transferred to the direct component benefit from a lower IAM loss coefficient.

- The spectral mismatch modifier translates for the gain/loss in irradiance because of the deviation in solar spectrum compared to the reference AM 1.5 standard spectrum and this is actually a gain in average for the study case. This correction is then displayed with negative values in the figure above. With regards to time, this modifier decreases, almost imperceptibly, according to the model presented in Section 2.3.3 since there is more precipitable water on average in the future projections because of of higher ambient temperatures.

- Soiling losses increase slightly with the median going up by 0.3% because of longer drought periods with too few rainfalls in future periods. More specifically, the median over all climate projections of the longest period between two 5mm/day rainfall episodes goes from 76 days on 1990-2020 to 93 days for 2050-2080.

- Temperature and aging losses increase because of a higher ambient

temperature average as expected but it is also the result of higher temperature peaks in the module during sunny hours.

- Inverter losses stay constant at 4.4 % over time since the overall DC production level does not significantly change.

Among all losses, temperature and aging losses have the highest variations and set the overall trend on the PR variations over time.

3.2. Impact of the PV temperature characteristics, orientation and location

PV systems can have a wide variety of design parameters that can influence their performances. In order to better evaluate their effect, different configurations are compared to the initial base case with regard to the temperature parameters, orientation, and location in France.

3.2.1. Impact of the temperature characteristics

The module losses can change due to different module technology sensitivity and building integration. In this section, two simulations are run to quantify those changes.

1. The first sets back γ, the efficiency loss coefficient to a more conservative -0.3%/°C.
2. The second simulation (BIPV) consists of modeling the building integration by changing the coefficients for the temperature model in Section 2.6 to $U_0 = 20\ \frac{W}{m^2K}$, $U_1 = 3.2\ \frac{W}{m^2K(m/s)}$ as suggested by PVGIS.[54]

The two simulations are compared in Figure 12 to the base case (orange) with the assumptions applied in the rest of the study with $\gamma = -0.45°C$ and

$U_0 = 26.9\ \frac{W}{m^2K}$, $U_1 = 6.2\ \frac{W}{m^2K(m/s)}$

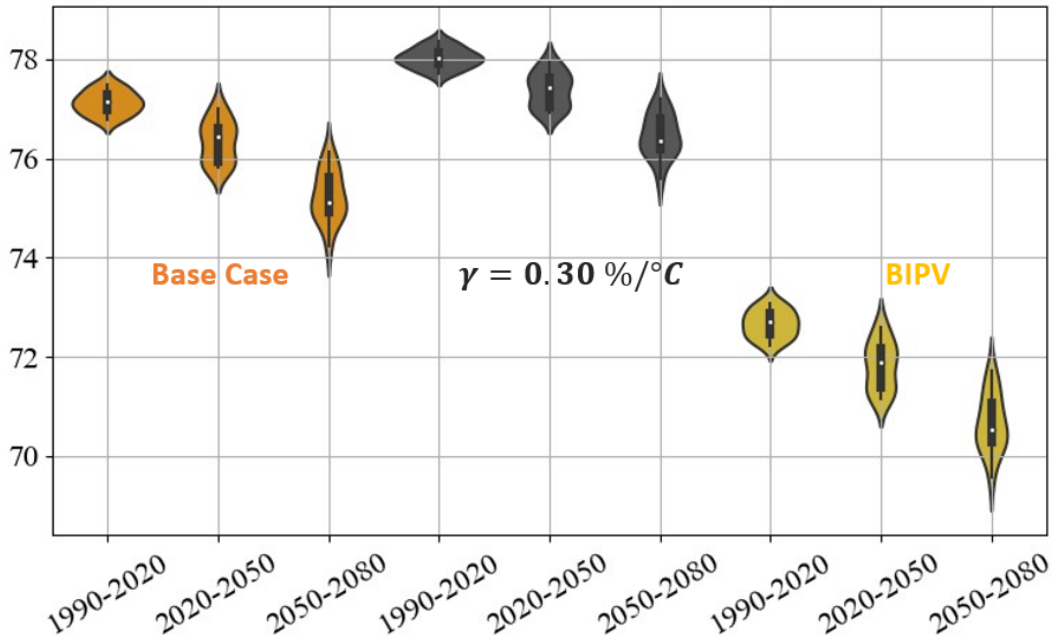

Figure 10: Performance Ratio over 30 years $\Delta_{PR}(period)$ on the 15 climate projections with different temperature parameters for different climate periods

Temperature losses are reduced when using a more conservative temperature coefficient, $\gamma = 0.30\%$, and the PR distribution is slightly higher than the base case. In regards to the evolution over time, the temperature loss variation between 1990-2020 and 2050-2080 is also reduced. However, the other losses such as aging, IAM/SMM, soiling etc. stay the same and the order of magnitude of the PR loss over time is nearly similar to the base case. In comparison to 1990-2020, the PR median decreases by 1.6 % when $\gamma = 0.30$ %/ °C and 2.0 % for the base case.

For the BIPV simulation, the temperature and aging losses are significantly higher and decrease the PR distribution median on 1990-2020 from 77.1 % (base case) to 72.7 %. A slightly more important decrease in performance between 2050-2080 and 1990-2020 is observed with the PR median decreasing by 2.1 % due to higher module temperatures. This decrease is similar to the base case in absolute numbers but is higher, relatively to the initial PR value and accentuates the effect of climate change .

3.2.2. Impact of the tilt and azimuth

In this section, the sensitivity of the installation orientation is studied. The performance losses between 2050-2080 and 1990-2020 have been computed for the 15 climate projections for different orientations as shown in Figure 11. More precisely, those are computed for realistic orientations with tilts and azimuths going from 0° to 90° and 60° to 300° respectively with a step of 5°.

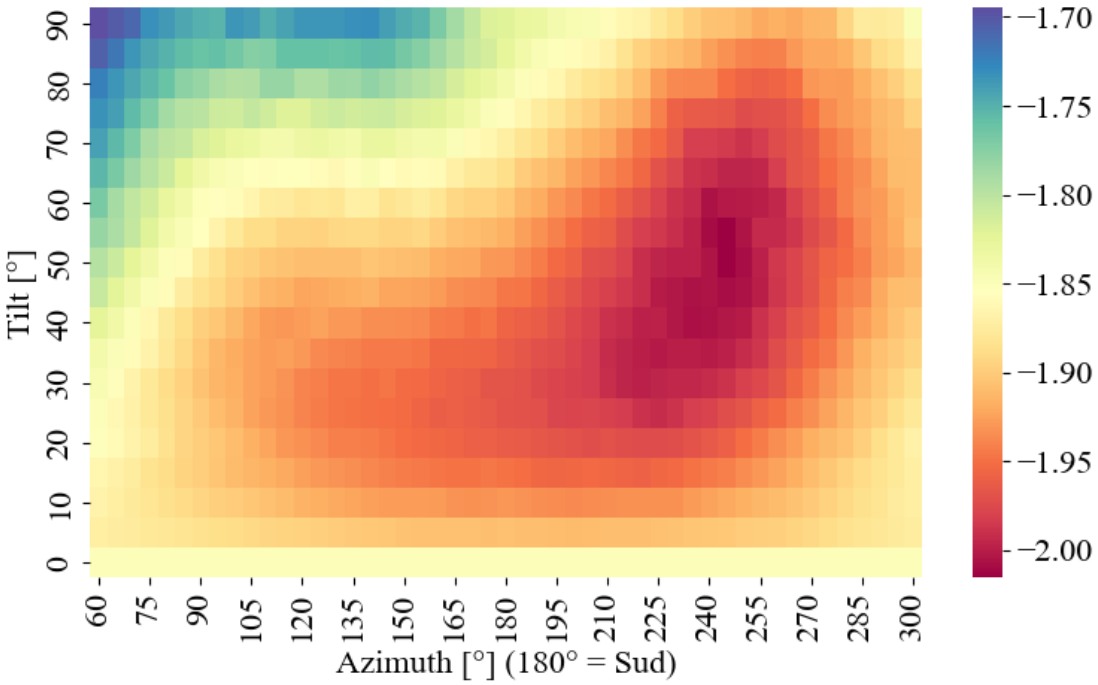

Figure 11: Performance Ratio loss on 2050-2080 compared to 1990-2020 (Distribution median) as function of the tilt and azimuth

Overall, the performance reduction ranges from 1.7 to 2 %. Some of the losses such IAM, SMM, soiling and inverter losses have globally a symmetric effect with regards to the orientation east/west. More specifically, IAM and SMM lead to slight differences compared to the base case when the angle of incidence becomes significant and small differences in the IAM and SMM factors induce higher changes on the performance. Next, soiling is usually larger in summer because of slightly longer drought periods than the rest of the year. Then, those losses become less variable over time with the orientations which make the irradiation more evenly distributed over the whole year. The variations in inverter losses over time as a function of the

orientation are negligible compared to the rest of the losses.

With regard to temperature and aging losses, those effects are a bit more asymmetric. This can be explained by the ambient temperature rise which becomes higher in the afternoon than in the morning on average over the fifteen climate projections. Then, the orientations which concentrate most of the received irradiation in the afternoon demonstrate higher temperature and aging losses than the base case. For instance, this particularly disadvantages installations that are orientated west which receive most of the irradiance at higher temperatures.

In the end, the orientation impacts the performance loss through different mechanisms but the overall order of magnitude is conserved around 1.9 - 2% for the most typical orientations facing somewhat south with low/moderate tilt.

3.2.3. Impact of the location in metropolitan France

The same methodology has been applied on four other cities in the French metropolitan territory to investigate potential different trends. In Table 5, the latitude, the longitude are collected, and the average module temperature when the irradiance is non-null and the PR^{p}_{30year}(1990-2020) distribution over all projections are computed over the whole lifetime on 1990-2020 for each city. The PR^{p}_{30year}(1990-2020) distributions on the recent past period differ softly from one city to the other according to their local environmental conditions. For instance, the most southern cities such as Nîmes and Bordeaux have lower PRs due to higher ambient temperatures while Paris and

Nantes have better PRs.

	Latitude / Longitude	**ERA5 dataset average daytime module temperature**	PR_{30year} **on 1990-2020** [%]		
			min	**median**	**max**
Paris	48.782 / 2.191	20.2°C	79.2	80.0	80.4
Nantes	47.183 / -1.617	21.4 °C	78.7	79.4	79.4
Grenoble	45.216 / 5.847	21.6 °C	77.5	78.2	78.5
Bordeaux	44.837 / -0.579	24.6 °C	76.8	77.1	77.3
Nîmes	43.762 / 4.416	26.6°C	76.2	76.8	77.3

Table 5: Coordinates and 30-year Performance Ratio PR_{30year} distribution of all climate projections on 1990-2020 of several metropolitan French cities

The relative performance ratios compared to 1990-2020 $\Delta^p_{PR}(period)$ for all climate projections are shown in Figure 12. Very similar trends are observed for all cities with a median decreasing by around 0.5-1% on 2020-2050 compared to 1990-2020 and 1.5-2% on 2050-2080.

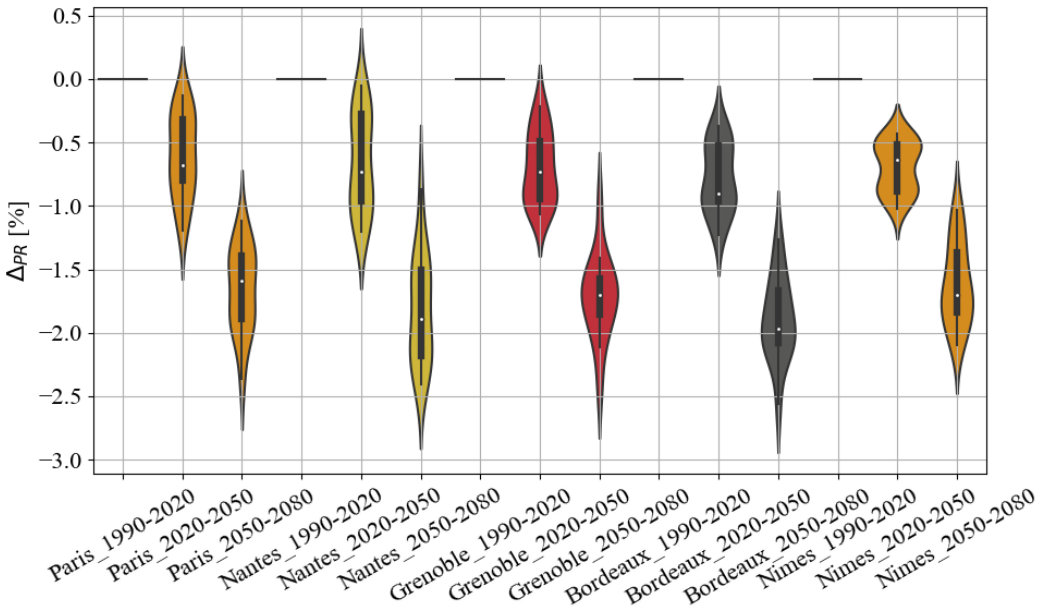

Figure 12: Relative Performance Ratio over 30 years $\Delta_{PR}(period)$ on the 15 climate projections for different climate periods compared 1990-2020

Some very slight differences still exist among the different cities which can be mostly explained by aging and soiling effects. For instance, Paris has a slightly smaller performance reduction than Nantes because Paris observes a smaller increase in module temperatures both in average and peaks. This particularly leads to a lower increase in aging losses for Paris through the degradation models exposed in Section 2.8. Also, one must note that the temperature losses increase less for Paris than Nantes for the same reasons but those loss variations between the two cities are negligible compared to the changes in aging losses.

Then soiling also participates to slightly differentiate the city performances. For example, Paris sees its drought periods slightly increasing in the future

but Bordeaux has much longer periods compared to the past and its impact on the performance over time is much more significant. The difference regarding the increase in soiling losses is in the order 0.1 % when comparing both cities.

However, from a general perspective, the order of magnitude of the performance losses over the different cities is very similar.

4. Discussion

The study has been focused on the effect of climate change in France for a mono-crystalline silicium open rack installation with a glass/polymer sandwich and aluminum frame, which is currently one of the most common technology. Quantifiable through the PhotoVoltaic Climate Zones (PVCZ) from Karin et al.,[55] the results could be extrapolated to other places with the same climate zone. France is mostly situated in the moderate climate within 'T3:H4' to 'T5:H4' zones (Cfb, Csa, Csb for Koppen Geiger climates) for the studied cities when inferring from coordinates for an open-rack mounted systems with Karin's tool.[56] Then, those results might also be applicable to other areas with the same climate zone which would witness the same increase in temperature such as most of the southern part of Europe, the top north of Africa and a portion of USA.

As exposed in Section 3.2.1, different module temperature configurations can slightly alter the end results and the heat island effect would potentially impact their amplitude. Unfortunately, the grid spacing of 8km from the ERA5 reanalysis is too large to take this local effect into account. Then, an

additional study with tools such as the urban weather generator to evaluate the effects of the heat island effect on the performance would potentially show more severe results because of higher temperature swings.

The model chain in Section 2 would also benefit from some uncertainty analysis. For instance, the NREL algorithm estimates the sun elevation and azimuth with a great accuracy of +/-0.0003° while the root mean square error from the transposition model could amount up to 100 W/m^2.[28] Also, the presented PVWatts model[50] is known to have some inaccuracy at low light levels. Then, some analysis would help to quantify which link has the highest degree of uncertainty in regards to the final results.

The chosen aging model from Kaaya et al.[43][51] was not built to study climate change on the PV system and ineluctably has some drawbacks. Model parameters are calibrated according to only one technology and might not be adapted to some others. Also, a yearly dynamic degradation rate taking into account the environmental conditions associated with a degradation-memory term would be more realistic to reflect the year-to-year variations due to aging.

The chosen degradation model from Kaaya et al.[43][51] also takes into account for module degradation only and considering system-level degradation would enable to have more representative insights. Those extra degradations could stem from inverter, curtailments, or protection devices (fuse, breakers) as mentioned by Bollinger et al..[7] Their effects are sometimes non-linear and their interactions with environmental conditions/time are complex to model.

Thus, the module accounts for an important share of the system degradation but an extra degradation layer reflecting the system degradation would potentially worsen the presented results.

Beyond the limitations listed above, failures and other losses are not included in this paper and these could play a significant role in performance. Usually assumed constant, mismatch and wiring losses have not been included in the study since it is assumed that they do not originate from meteorological features and would not vary from different environment conditions because of climate change.

However, on the AC side, more hot hours would make the inverter operate under temperature derating and reduce temporarily the total performance of the photovoltaic installation. Higher ambient temperatures would also speed up the inverter's end of life from a reliability perspective[57].[58]

On the DC side, more frequent and severe failures might also appear in warmer conditions and decrease the performance. According to Aghaei et al.,[59] some of the primary stress factors affecting PV reliability include irradiance, temperature, moisture and chemicals. Several failures models such as PID,[60] LID or LeTID[61] incorporate the module temperatures and humidity as inputs and would increase the power loss under warmer conditions. Also, constant high temperatures are detrimental to bypass diode and junction box function and can increase failure rates.[62]

Then, investigating the climate change effects on failures would complete this study to more accurately assess PV performance in warmer weather conditions.

While climate change affects module performance, future technologies might also be more and more resilient to climate change. Motivated by market competition, PV suppliers aim at producing PV panels with longer lifetimes and lower sensitivity to module temperature. Then, the effect of climate change on the performance might even more be reduced due to those improvements.

5. Conclusion

In this article, a model chain was established in order to propagate climate projections and quantify the effect of climate change on photovoltaic performance for any installation. To this end, the hourly AC power production taking into account natural aging was obtained through a collection of models that were used to estimate the Performance Ratio, the standard measure, to compare PV performance over different periods of time. Long-term increases in ambient temperatures due to climate change were shown to reduce energy generation mainly through two factors: instantaneous decreases in yield due to a negative temperature coefficient and accelerating natural aging mechanisms that are temperature dependent. In the presented case studies, longer drought periods in the future also seem to enhance soiling losses due to a lower natural cleaning frequency from the precipitations.

The performance of a mono-crystalline open-rack photovoltaic installation was simulated in different cities in France in the close past period 1990-2020, the near future 2020-2050, and ahead to 2050-2080 following the most

pessimistic climate scenario RCP 8.5. It was found that the aging component varies at most by 0.9 % in the furthest projection period compared to the recent past period and that the instantaneous temperature-dependent component has a negative impact on the performance with a 1% and 2.2% decrease after 30 years of operation on 2020-2050 and 2050-2080 respectively at Bordeaux. On top of that, the year-to-year variation of the instantaneous performance component has a tendency to increase over time. When looking at some other cities in France, a decrease of less than 3% was observed in the performance ratio for almost all projections. Overall, it can be concluded that the effect of climate change in the regions studied and through the mechanisms explored in this study are limited in magnitude.

Acknowledgements

The authors thank the ANRT funding and the co-funding between Heliocity and CSTB for the project "Methodology development to guarantee building photovoltaic systems' performance including failure modeling". This work has been supported by the French National Research Agency, through the Investments for Future Program (ref. ANR 18 EURE 0016 Solar Academy).

A. Appendix: climate data processing

Fifteen climate models are extracted from EURO-CORDEX-11 and are bias-corrected to fit the variable distributions on the reference period 1981-

2019 on the ERA5 dataset of the chosen location. Then, the three-hourly time series are converted into hourly in order to be ready to be injected in the models Section 2.

A.1. Used climate projections

Table 6 describes the global and regional models used for the 15 models in this study.

A.2. Bias correction

In order to correct the bias in climate model outputs because of the location constraints, two bias correction methods of the quantile-quantile correction type are adopted: the Q-MAP and the CDF-t methods. The general principle is to correct the distribution of a variable of the climate model output using the distribution of the same variable from the reference dataset on the reference period 1981-2019.
To avoid introducing a bias during the correction, the correction methods are applied over the periods by month and by hour for each variable in order to eliminate the seasonal and diurnal cycles.

A.2.1. The Q-MAP method

For any selected period, reference or other, the Q-MAP[23–25] method corrects a distribution quantile by quantile so that the quantiles match those of the reference distribution. If it is assumed that the distribution on future periods is the same as the reference, this method is particularly suited.

As for the method, let F_{ref} be the cumulative density function (CDF) of the reference dataset ERA5 of a climate variable, such as temperature, over

Driving Global Climate Model (realization)	**Regional Climate Model**	**Institute**
ICHEC-EC-EARTH (r1i1p1)	COSMO-crCLIM-v1-1	Zurich Federal Institute of Technology (ETH Zurich)
ICHEC-EC-EARTH (r1i1p1)	RegCM4-6	Abdus Salam International Centre for Theoretical Physics (ICTP)
ICHEC-EC-EARTH (r1i1p1)	RACMO22E	Royal Netherlands Meteorological Institut (KNMI)
ICHEC-EC-EARTH (r1i1p1)	RCA4	Swedish Meteorological and Hydrological Institute (SMHI)
IPSL-IPSL-CM5A-MR (r1i1p1)	RACMO22E	Royal Netherlands Meteorological Institut (KNMI)
IPSL-IPSL-CM5A-MR (r1i1p1)	RCA4	Swedish Meteorological and Hydrological Institute (SMHI)
MOHC-HadGEM2-ES (r1i1p1)	ALADIN63	Centre National de Recherches Météorologiques (CNRM)
MOHC-HadGEM2-ES (r1i1p1)	RACMO22E	Royal Netherlands Meteorological Institut (KNMI)
MOHC-HadGEM2-ES (r1i1p1)	RCA4	Swedish Meteorological and Hydrological Institute (SMHI)
MPI-M-MPI-ESM-LR (r1i1p1)	ALADIN63	Centre National de Recherches Météorologiques (CNRM)
MPI-M-MPI-ESM-LR (r1i1p1)	RegCM4-6	Abdus Salam International Centre for Theoretical Physics (ICTP)
MPI-M-MPI-ESM-LR (r1i1p1)	RACMO22E	Royal Netherlands Meteorological Institut (KNMI)
NCC-NorESM1-M (r1i1p1)	COSMO-crCLIM-v1-1	Zurich Federal Institute of Technology (ETH Zurich)
NCC-NorESM1-M (r1i1p1)	ALADIN63	Centre National de Recherches Météorologiques (CNRM)
NCC-NorESM1-M (r1i1p1)	RegCM4-6	Abdus Salam International Centre for Theoretical Physics (ICTP)
NCC-NorESM1-M (r1i1p1)	RCA4	Swedish Meteorological and Hydrological Institute (SMHI)

Table 6: EURO-CORDEX models

the reference period 1981-2019. More specifically, the function F_{ref} indicates the probability that a value X is less than or equal to a value x, where $F_{ref}(x) = \mathbb{P}_X(X \leq x)$. In the same way, F_{mod} is the CDF of one of the climate models on the same variable and period. Then for all model values x_{mod}, it exists a reference value x_{ref} so that

$$F_{ref}(x_{ref}) = F_{mod}(x_{mod}) \tag{35}$$

From this relation, the transfer function T can be deducted based on CDFs on the common reference time period 1981-2019 and the T function can then be applied to the same variable on future periods of the climate model.

$$T = (F_{ref}^{-1} \circ F_{mod}) \tag{36}$$

A.2.2. The CDF-t method

The CDF-t (Cumulative Density Function - transform)[22] can be seen as a variant of the Q-MAP method but it differs by allowing distribution changes over time. The CDF-t method conserves the relative variations over time of the cumulative density function of the climate model variable before correction and after correction.

From a modeling perspective, let F_{ref}^{H} be the reference cumulative distribution function of an ERA5 variable over the reference period 1981-2019. Similarly, let F_{mod}^{H} and F_{mod}^{F} be the CDFs of the same variable from a climate model over the reference period 1981-2019 and over a future period respectively.

It is possible to obtain the reference CDF F_{ref}^{F} on the future period since the evolution of the CDFs over time must be respected with the following equation

$$(F_{mod}^{F})^{-1} \circ F_{mod}^{H} = (F_{ref}^{F})^{-1} \circ F_{ref}^{H} \tag{37}$$

By recombining the Equation 37, it is possible to find the bias-corrected CDF F_{ref}^{F} and later find the transfer function as for the Q-MAP method.

$$F_{ref}^{F} = F_{ref}^{H} \circ \left(F_{mod}^{H}\right)^{-1} \circ F_{mod}^{F} \tag{38}$$

The CDF-t method is a non-stationary bias correction method that takes into account a change in the distribution of the variable over time, which is not possible with the Q-MAP method.

Hourly interpolation

Since hourly values are needed for the model chain Section 2, the bias-corrected climate projections are post-processed with a Hermite cubic interpolation[26,27] into hourly values.

It is important to note that this interpolation from three-hourly to hourly data can introduce a bias in the auto-correlation of wind speeds, with potentially higher final auto-correlations than in the hourly reference data. Also, one must note that ERA5 wind data have a defect in the diurnal cycle (as mentioned in ERA5 documentation[21]), which may induce a bias in the diurnal cycle of the final wind speeds obtained.

References

[1] G. Masson, I. Kaizuka, Trends in Photovoltaic Applications, IEA-PVPS T1-41:2021, **2021**.

[2] I. R. E. Agency, World Energy Transition Outlook: 1.5 °C Pathway, IRENA, **2021**.

[3] E. Union, DIRECTIVE (EU) 2018/844, **2018**.

[4] C. Deline, K. Anderson, D. Jordan, A. Walker, J. Desai, K. Perry, M. Muller, B. Marion, R. White, **2021**.

[5] B. Meng, R. C. G. M. Loonen, J. L. M. Hensen, *Appl. Energy* **2022**, *322*, 119550.

[6] D. C. Jordan, K. Anderson, K. Perry, M. Muller, M. Deceglie, R. White, C. Deline, *Prog. Photovoltaics* **2022**, *30*, 1166.

[7] M. Bolinger, W. Gorman, D. Millstein, D. Jordan, *J. Renewable Sustainable Energy* **2020**, *12*, 043501.

[8] N. Bansal, S. P. Jaiswal, G. Singh, *Sustain. Energy Technol. Assess.* **2021**, *47*, 101526.

[9] T. Nordmann, L. Clavadetscher, W. G. v. Sark, M. Green, Analysis of Long-Term Performance of PV System, Technical Report IEA-PVPS T13-05:2014, **2014**.

[10] D. C. Jordan, S. R. Kurtz, K. VanSant, J. Newmiller, *Prog. Photovoltaics* **2016**, *24*, 978.

[11] S. Lindig, J. Ascencio-Vásquez, J. Leloux, D. Moser, A. Reinders, *IEEE J. Photovolt.* **2021**, *11*, 1312.

[12] J. Leloux, L. Narvarte, D. Trebosc in Proc. 26th European Photovoltaic Solar Energy Conference and Exhibition, Hamburg, Germany, **2011**.

[13] S. Jerez, I. Tobin, R. Vautard, J. P. Montávez, J. M. López-Romero, F. Thais, B. Bartok, O. B. Christensen, A. Colette, M. Déqué, G. Nikulin, S. Kotlarski, E. van Meijgaard, C. Teichmann, M. Wild, *Nat. Commun.* **2015**, *6*, 10014.

[14] G. Narvaez, L. Giraldo, M. Bressan, A. Pantoja, *Heliyon* **2022**, *8*, e11122.

[15] J. Ascencio-Vasquez, K. Ismail, K. Brecl, K.-A. Weiss, M. Topic, *Energies* **2019**, *12*, 4749.

[16] J. Ascencio-Vásquez, K. Brecl, M. Topič, *Sol. Energy* **2019**, *191*, 672.

[17] W. F. Holmgren, C. W. Hansen, M. A. Mikofski, *J. Open Source Softw.* **2018**, *3*, 884.

[18] F. Giorgi, C. Jones, G. Asrar, *WMO Bull* **2008**, *58*, 175.

[19] D. Jacob, J. Petersen, B. Eggert, A. Alias, O. Christensen, L. Bouwer, A. Braun, A. Colette, M. Déqué, G. Georgievski, E. Georgopoulou, A. Gobiet, L. Menut, G. Nikulin, A. Haensler, N. Hempelmann, C. Jones, K. Keuler, S. Kovats, P. Yiou, *Reg. Environ. Change* **2014**, *14*, 563.

[20] D. Randall, R. Wood, S. Bony, R. Colman, T. Fichefet, J. Fyfe, V. Kattsov, A. Pitman, J. Shukla, J. Srinivasan, S. Ronald, A. Sumi, K. Taylor, *Climate Change 2007: The Physical Science Basis*, Cambridge University Press, **2007**.

[21] H. Hersbach, B. Bell, P. Berrisford, S. Hirahara, A. Horányi, J. Muñoz-Sabater, J. Nicolas, C. Peubey, R. Radu, D. Schepers, A. Simmons, C. Soci, S. Abdalla, X. Abellan, G. Balsamo, P. Bechtold, G. Biavati, J. Bidlot, M. Bonavita, G. De Chiara, P. Dahlgren, D. Dee, M. Diamantakis, R. Dragani, J. Flemming, R. Forbes, M. Fuentes, A. Geer, L. Haimberger, S. Healy, R. J. Hogan, E. Hólm, M. Janisková, S. Keeley, P. Laloyaux, P. Lopez, C. Lupu, G. Radnoti, P. de Rosnay, I. Rozum, F. Vamborg, S. Villaume, J.-N. Thépaut, *Q. J. R. Meteorol. Soc.* **2020**, *146*, 1999.

[22] P.-A. Michelangeli, M. Vrac, H. Loukos, *Geophys. Res. Lett.* **2009**, *36*.

[23] H. Panofsky, G. Brier, *Some Applications of Statistics to Meteorology*, Earth, Mineral Sciences Continuing Education, College of Earth, and Mineral Sciences, **1968**.

[24] A. Wood, L. Leung, V. Sridhar, D. Lettenmaier, *Clim. Change* **2004**, *62*, 189.

[25] M. Déqué, *Glob. Planet. Change* **2007**, *57*, 16.

[26] J. M. Hyman, *SIAM J. Sci. Comput.* **1983**, *4*, 645.

[27] R. L. Dougherty, A. S. Edelman, J. M. Hyman, *Math. Comput.* **1989**, *52*, 471.

[28] R. Perez, P. Ineichen, E. Maxwell, R. Seals, A. Zelenka, *ASHRAE Trans* **1992**, *98*, 354.

[29] J. W. Spencer, *Search* **1971**, *2*, 162.

[30] F. Kasten, A new table and approximation formula for the relative optial air mass, CRREL, **1966**.

[31] E. E. Agency, Copernicus Land Monitoring Service - EU-DEM, **2017**.

[32] I. Reda, A. Andreas, *Sol. Energy* **2004**, *76*, 577.

[33] R. Perez, P. Ineichen, R. Seals, J. Michalsky, R. Stewart, *Sol. Energy* **1990**, *44*, 271.

[34] PVsyst – Photovoltaic Software, https://www.pvsyst.com/, accessed in Oct, **2023**.

[35] N. Martin, J. Ruiz, *Sol. Energy Mater. Sol. Cells* **2001**, *70*, 25.

[36] K. Ilse, L. Micheli, B. W. Figgis, K. Lange, D. Daßler, H. Hanifi, F. Wolfertstetter, V. Naumann, C. Hagendorf, R. Gottschalg, J. Bagdahn, *Joule* **2019**, *3*, 2303.

[37] A. Kimber, L. Mitchell, S. Nogradi, H. Wenger in Proc. IEEE 4th World Conference on Photovoltaic Energy Conference, *Vol. 2*, Waikoloa, HI, USA, **2006**, p. 2391.

[38] J. G. Bessa, L. Micheli, F. Almonacid, E. F. Fernández, *iScience* **2021**, *24*, 102165.

[39] M. Lee, A. Panchula in Proc. 43rd IEEE Photovoltaic Specialists Conference, Portland, USA, **2016**, p. 1351.

[40] C. Gueymard, *SMARTS2, a simple model of the atmospheric radiative transfer of sunshine: algorithms and performance assessment*, Florida Solar Energy Center, **1995**.

[41] C. Gueymard, *Sol. Energy* **1994**, *53*, 57.

[42] D. Bolton, *Mon. Weather Rev.* **1980**, *108*, 1046.

[43] I. Kaaya, M. Köhl, A.-P. Mehilli, M. Sidrach-de-Cardona, K. Weiss, *IEEE J. Photovolt.* **2019**, *9*, 1105.

[44] D. Crommelynck, A. Joukoff, *Sol. Energy* **1990**, *45*, 131.

[45] J. Remund, L. Wald, M. Lefèvre, T. Ranchin, J. Page in Proc. ISES Solar World Congress 2003, Goteborg, Sweden, **2003**.

[46] P. Ineichen, R. Perez, *Sol. Energy* **2002**, *73*, 151.

[47] D. Faiman, *Prog. Photovoltaics* **2008**, *16*, 307.

[48] I. Kaaya, PhD Thesis, University of Malaga, **2020**.

[49] K. Michael, H. Markus, W. Stefan, W. Jochen, *Sol. Energy Mater. Sol. Cells* **2011**, *95*, 1638.

[50] A. P. Dobos, PVWatts Version 5 Manual, **2014**.

[51] I. Kaaya, J. Ascencio-Vásquez, K.-A. Weiss, M. Topič, *Sol. Energy* **2021**, *218*, 354.

[52] K.-A. Weiss, L. S. Bruckman, R. H. French, G. Oreski, T. Tanahashi, Service Life Estimation for Photovoltaic Modules, IEA-PVPS T13-16:2021, **2021**.

[53] IEC 61724-1: Photovoltaic system performance monitoring, **2021**.

[54] T. Huld, R. Müller, A. Gambardella, *Sol. Energy* **2012**, *86*, 1803.

[55] T. Karin, C. Jones, A. Jain in Proc. 46th IEEE Photovoltaic Specialist Conference, Chicago, IL, USA, **2019**, p. 0687.

[56] T. Karin, Photovoltaic Climate Zones and Stressors, `https://github.com/toddkarin/pvcz`, **2019**.

[57] A. Nagarajan, R. Thiagarajan, I. L. Repins, P. L. Hacke, Photovoltaic Inverter Reliability Assessment, **2019**.

[58] B. Zhang, Y. Gao, *Microelectron. Reliab.* **2023**, *147*, 115073.

[59] M. Aghaei, A. Fairbrother, A. Gok, S. Ahmad, S. Kazim, K. Lobato, G. Oreski, A. Reinders, J. Schmitz, M. Theelen, P. Yilmaz, J. Kettle, *Renewable Sustainable Energy Rev.* **2022**, *159*, 112160.

[60] P. Hacke, S. Spataru, K. Terwilliger, G. Perrin, S. Glick, S. Kurtz, J. Wohlgemuth, *IEEE J. Photovolt.* **2015**, *5*, 1549.

[61] M. Woodhouse, I. Repins, D. Miller, LID and LeTID Impacts to PV Module Performance and System Economics DRAFT Analysis, Presented at DuraMAT Webinar, 14 Dec, USA, **2020**.

[62] M. Herz, G. Friesen, U. Jahn, M. Köntges, S. Lindig, D. Moser, Quantification of Technical Risks in PV power Systems, IEA-PVPS T13-23:2021, **2022**.